

# FastMap: Fast Queries Initialization Based Vectorized HD Map Reconstruction Framework

Haotian Hu

hu.haotian@leapmotor.com

Jingwei Xu

xu.jingwei@leapmotor.com

Fanyi Wang

11730038@zju.edu.cn

Toyota Li

independent

Yaonong Wang

wang-yaonong@leapmotor.com

Laifeng Hu

hu\_laifeng@leapmotor.com

Zhiwang Zhang

zhiwang.zhang@nit.zju.edu.cn

## Abstract

*Reconstruction of high-definition maps is a crucial task in perceiving the autonomous driving environment, as its accuracy directly impacts the reliability of prediction and planning capabilities in downstream modules. Current vectorized map reconstruction methods based on the DETR framework encounter limitations due to the redundancy in the decoder structure, necessitating the stacking of six decoder layers to maintain performance, which significantly hampers computational efficiency. To tackle this issue, we introduce **FastMap**, an innovative framework designed to reduce decoder redundancy in existing approaches. FastMap optimizes the decoder architecture by employing a single-layer, two-stage transformer that achieves multilevel representation capabilities. Our framework eliminates the conventional practice of randomly initializing queries and instead incorporates a heatmap-guided query generation module during the decoding phase, which effectively maps image features into structured query vectors using learnable positional encoding. Additionally, we propose a geometry-constrained point-to-line loss mechanism for FastMap, which adeptly addresses the challenge of distinguishing highly homogeneous features that often arise in traditional point-to-point loss computations. Extensive experiments demonstrate that FastMap achieves state-of-the-art performance in both nuScenes and Argoverse2 datasets, with its decoder operating  $\times 3.2$  faster than the baseline. Code and more demos are available at <https://github.com/hht1996ok/FastMap>.*

## 1. Introduction

The high definition map serves as an environmental prior knowledge base for autonomous driving systems, provid-

ing foundational support for key modules such as vehicle localization, trajectory prediction, and motion planning through precise road topology modeling and traffic rule encoding. Traditional off-line mapping solutions based on SLAM [20, 21], while capable of building centimeter-level accuracy maps, rely on specialist collection equipment and manual post-processing, resulting in high costs that make it difficult to meet the mass production demands of autonomous driving. In recent years, significant progress has been made in the field of online high-definition map reconstruction technologies based on in-vehicle surround-view cameras [4, 8, 10–12, 14, 23, 25]. These technologies have achieved real-time vectorized map generation in dynamic environments through visual BEV (Bird’s Eye View) representation learning. Among these, the DETR-style [3, 26, 30] decoding paradigm established by MapTR [13] and its derivative works [8, 14, 19] have become the mainstream solution.

Despite significant progress that has been made, existing methods still face two core challenges: the efficiency bottleneck of the decoder and the issue of forcibly fitting predicted points to annotated points. Specifically, methods such as MapTR [13] require the stacking of six decoder layers to ensure the accuracy of the prediction of the map elements. This is achieved by progressively refining the randomly initialized query vectors through layer-by-layer optimization. Although this design improves the representation capabilities of the model, it results in a substantial increase in the number of model parameters and the computational load, severely constraining deployment efficiency. Due to computational constraints of onboard vehicle chips, in-vehicle models are typically limited to use only one or two decoder layers, which results in substantial degradation in their accuracy. Recent methods, such as TransFusion [1], have demonstrated in 3D detection tasks that a single-layer

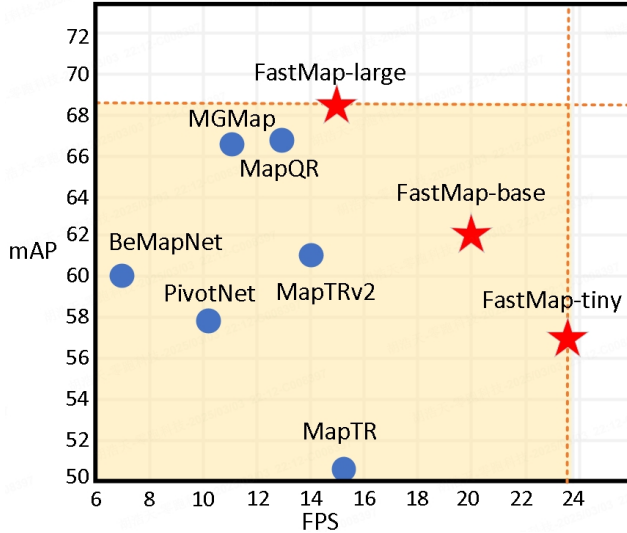


Figure 1. Comparison graphs of mAP and FPS between FastMap and existing models.

decoder can achieve performance comparable to multilayer cascaded structures through feature-guided query initialization strategies, providing new insights for efficient decoder design. However, its applicability in vectorized map reconstruction remains to be validated, and suitable query initialization methods are required to adapt to the unique shapes of map instances. Furthermore, despite the obvious lack of semantic differences between vector points on map elements, the existing supervised paradigm forces the model to adapt to manually annotated vector point coordinates. Forcing the alignment of predicted points with ground-truth points would impose too strict constraints on the model’s output, to the detriment of the learning process.

To address these challenges, this paper innovatively proposes an efficient vector map reconstruction framework called FastMap. The FastMap decoder uses only a single-layer, two-stage structure of the transformer, and we implement a cross-modal attention mechanism for intelligent initialization of query vectors through the heatmap-guided query generation module. Specifically, the FastMap decoder generates initialized map queries with geometric prior through BEV feature cross-attention in the first stage, replacing the traditional random initialization approach. In the second stage, it leverages the positional information between map queries and image BEV features as a prior to directly generate reference points within the ROI for further refinement and enhancement of map element features. At the supervision level, we propose the FastMap loss based on point-to-line distance, establishing supervision signals by minimizing the distance from predicted points to ground truth curves. This effectively mitigates the adverse effects

of forcibly fitting predicted points to annotated points.

We validated the efficiency and effectiveness of FastMap in the nuScenes [2] and Argoverse2 [24] datasets. As shown in Figure 1, FastMap-large achieved the best performance compared to sota methods, reaching 68.1 mAP in the nuScenes benchmark. Furthermore, FastMap-base exhibited substantial superiority over MapTRv2, enhancing mAP while concomitantly increasing the inference speed by 40.3%. Our contributions are summarized as follows:

- We propose a framework that employs heatmap to rapidly initialize map queries, which enables our method to achieve better performance using a single layer decoder than the multilayer decoder baselines.
- We construct a point-to-line based loss mechanism, which is different from the traditional point-by-point coordinate regression based method whose accuracy is largely affected by the accuracy of heatmap. Our method constrains the spatial positions by strictly matching the predicted and labeled points, and transforms the optimization objective into minimizing the distance from the predicted points to the target curve.
- FastMap significantly improves model inference speed while maintaining model accuracy. Especially for in-vehicle applications, it can greatly enhance online map quality with a negligible increase in time consumption.

## 2. Related Work

### 2.1. BEV Perception Decoder

In the domain of BEV perception, the decoder serves as a key component, exerting a direct influence on the accuracy of the target geometry and the recovery of semantic information. DETR [3] pioneered the integration of the Transformer architecture into 2D detection tasks, employing multilayer decoders to iteratively refine the learnable query. Nevertheless, its sluggish convergence and computational inefficiency are exacerbated in 3D contexts. To mitigate the efficiency bottleneck, Efficient DETR [26] leverages sliding windows to extract dense region proposals from image features and selects candidate boxes as initial object queries based on confidence scores, thus substantially reducing the required number of decoder layers. TransFusion [1] demonstrated the efficacy of a feature-guided query initialization strategy in 3D object detection, achieving an accuracy comparable to multilayer structures with a single-layer decoder, thus charting a novel trajectory for efficient decoder design. However, its applicability and potential in the reconstruction of vectorized maps remain unexplored.

### 2.2. Online High Definition Map Reconstruction

With the increasing demand for online mapping, end-to-end vectorized map reconstruction has emerged as a prominent research focus. VectorMapNet [16] pioneered direct regres-

sion from multiview images to vector map elements, employing an autoregressive decoder to sequentially predict polygon vertices. However, this approach exhibits sensitivity to the direction of point sequences and suffers from limited inference speed. MapTR [13] mitigated the ambiguity of point order through symmetric permutation equivalence modeling and incorporated a DETR-style matching mechanism to enhance convergence efficiency, yet it remains constrained by the computational overhead of a six-layer decoder. HMap [29] introduced hybrid queries to jointly model element-level and point-level features, augmenting local details through interactive attention mechanisms. HRMapNet [28] integrated historical raster map priors, utilizing temporal information to improve reconstruction consistency.

### 3. Method

#### 3.1. Overall framework

The proposed FastMap is shown in Figure 2, which establishes an end-to-end framework from multi-camera inputs to road element sensing. Backbone is used to extract image features and view transformer is used to transform multi-view features into BEV space to get BEV feature  $F_{BEV}$ . The FastMap decoder employs a two-stage architecture that progressively refines the interaction between the query and the BEV features, ultimately generating map instances. FastMap loss mechanism is implemented to constrain the model predictions, thus addressing the challenge of ambiguous associations between ground truth points and semantic features.

#### 3.2. FastMap Decoder

Following the setting of MapTR [13], we randomly initialized the query  $n * m$  instance points to represent map instances and intra-instance points, where  $n$  denotes the number of map instances and  $m$  denotes the number of predicted points within each instance. The queries and query positions are represented as  $Q_{feat}^{init}$  and  $Q_{pos}^{init}$ , respectively. To ensure that initialized queries are endowed with rich semantic and positional information, FastMap implements a two-stage map instance decoder. In the first stage of the decoder, the heatmap-guided query generation module is used to regionally focus the BEV features using the ROI feature extraction strategy and to generate the coarse-grained map embedding  $F_{coarse}$  using the sparse features efficiently. The Coarse-Grained Cross-Attention (CGCA) and geometric prior generation strategy are included in this module. The output embedded features contain semantic and location information of the instances, providing support for the reference point coordinates required for the second stage of multi-scale deformable attention.

In the second stage of the decoder, we designed a Fine

Grained Cross-Attention (FGCA) to facilitate deep interaction between the coarse-grained features and the complete BEV features. This module effectively mitigates the potential loss of detail caused by ROI extraction through a feature compensation mechanism, ultimately producing map instance features  $F_{fine}$  with complete geometric details and semantic information. This two-stage coarse-to-fine decoding architecture significantly enhances the modeling capability of complex road topologies while maintaining computational efficiency.

##### 3.2.1. Heatmap GT Generation

As shown in Figure 3, to accurately extract ROI from the BEV features, we develop multicategory-aware instance heatmap ground truths specifically designed for different categories of map elements. These ground truths are generated by discretizing annotated points and their topological connections. We identify the pixels where the ground truth points are located and the regions encompassed by the connecting lines of adjacent points as positive samples. Furthermore, we utilize a Gaussian kernel to achieve pixel expansion, dynamically balancing the ratio of positive to negative samples by adjusting the kernel radius.

##### 3.2.2. Geometric Prior Generation

The BEV features are processed using a multilayer convolutional network to generate a heatmap, which is then utilized to filter candidate ROI regions based on a confidence threshold. Concurrently, the characteristics of the corresponding geometric prior  $F_{sam}$  and their spatial coordinates  $P_{sam}$  are also outputted. To address the problem of missed detection of distant instances caused by traditional uniform sampling, we propose a Circular Sampling Method (CSM). CSM divides the BEV plane into three concentric circular regions, labeled  $L_1$  to  $L_3$ . A progressive sampling rule is designed based on the distance relationship between the edges of the circular rings and the center of the BEV: the sampling ratio for the outermost largest ring ( $L_3$ ) is  $M \times \frac{L_3}{L_1+L_2+L_3}$ , while the ratio for the innermost smallest ring ( $L_1$ ) is  $M \times \frac{L_1}{L_1+L_2+L_3}$ , where  $M$  represents the total number of sampling points. This approach ensures a more balanced and effective sampling strategy across different regions of the BEV plane.

##### 3.2.3. Coarse Grained Cross-Attention

Typically, random initialization of the query position generates reference points that make it difficult for deformable attention to capture the correct spatial location, which means that the model needs more training rounds to learn the offsets. To address this issue, we propose the CGCA. This module constructs coarse-grained map embeddings  $F_{coarse}$  by associating with the  $M$  sparse sampling points output by the CSM. These sampling points provide the queries with approximate positional and semantic information. Con-

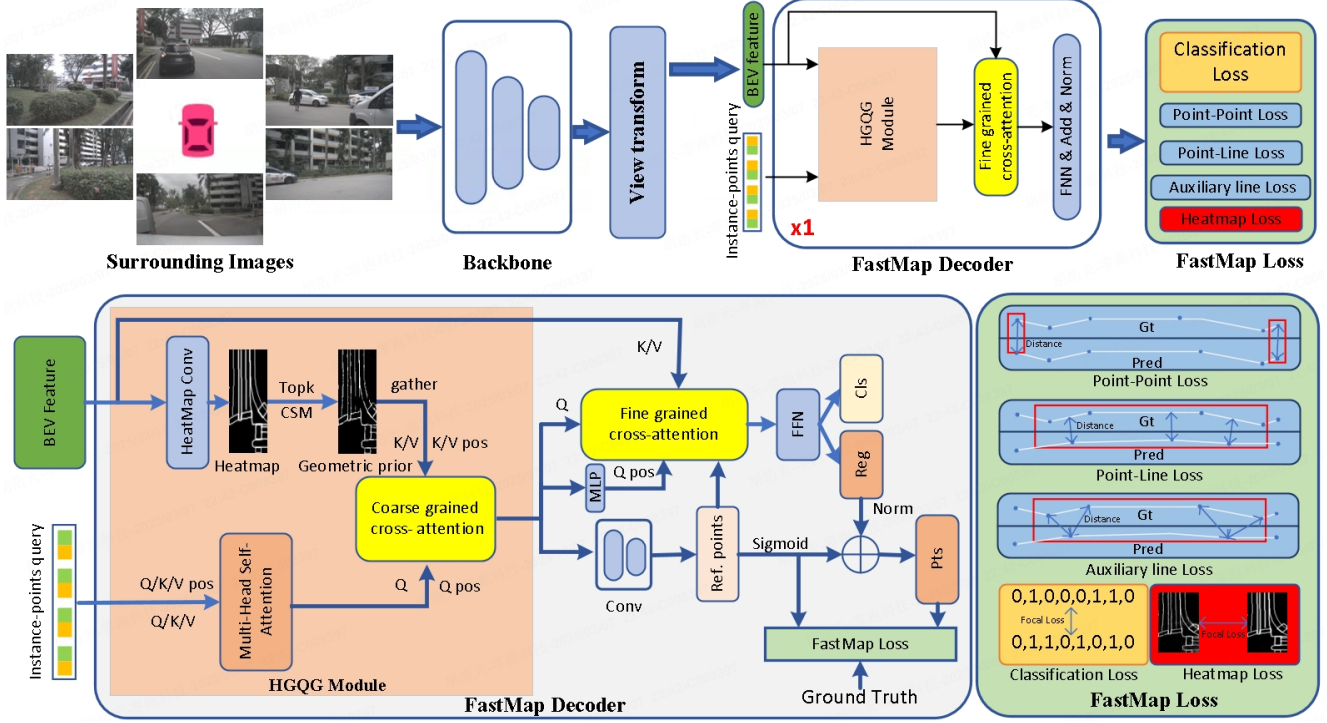


Figure 2. Overall Framework of FastMap. The Decoder Position illustrates how positional information is propagated in the decoder for queries, keys, and values. TopK represents the operation of identifying the Top-K elements with the largest values. CSM denotes the Circular Sampling Method. HGQG Module denotes heatmap-guided query generation module. Gather refers to the operation of extracting elements based on indices. Norm indicates the normalization operation performed according to spatial length.

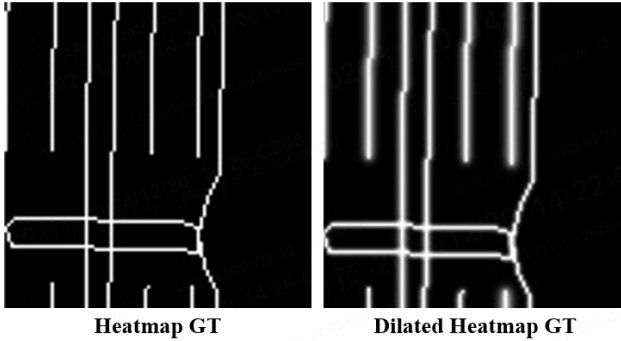


Figure 3. Heatmap ground truth visualisation before and after inflation.

sequently, the reference points generated on the basis of the coarse-grained embeddings enable the attention mechanism to focus on key regions even during the initial training stages. The pipeline of the decoder can be simply formu-

lated as:

$$K_{pos} = W_p P_{sam}, \quad (1)$$

$$K_{feat} = F_{sam} + W_c Cls, \quad (2)$$

where  $K_{pos}$  represents the key positions input to the Cross-Attention,  $K_{feat}$  denotes the input key features, and  $Cls$  signifies the category information in the heatmap. Subsequently, the coarse-grained instance features  $F_{coarse}$  are computed as follows:

$$K_{coarse} = K_{feat} + K_{pos}, \quad (3)$$

$$F_{coarse} = CA(Q_{pos}^{init}, K_{coarse}, K_{coarse}). \quad (4)$$

In  $CA()$ , the inputs are provided in the order of query, key and value to the Cross-Attention.

### 3.2.4. Fine Grained Cross-Attention

The selected sampling points may not fully encompass the details within the road elements, which requires further refinement of the map features. The FGCA consists of several MLPs and a multi-scale deformable attention. To facilitate its more effective convergence, the coarse-grained features  $F_{coarse}$  are projected through MLP to generate fine-grained

query coordinates and reference point offsets. Concurrently, the BEV features, which are rich in multi-modal scene characteristics, are input as the key and value for the attention mechanism. The fine-grained instance features  $F_{fine}$  are represented as follows:

$$Q_{pos} = W_q F_{coarse}, \quad (5)$$

$$R_{ref} = \text{Sigmoid}(W_{ref} F_{coarse}), \quad (6)$$

$$F_{fine} = \text{MSDeformAttn}(Q_{pos}, R_{ref}, F_{BEV}). \quad (7)$$

In this context, the  $\text{MSDeformAttn}()$  function takes inputs in the order of query, reference point, and value. Here,  $F_{BEV}$  represents the BEV features,  $Q_{pos}$  denotes the fine-grained query coordinates generated from the coarse-grained features,  $W_q$  represents the MLP weights, and  $R_{ref}$  represents the normalized reference points.

### 3.3. FastMap Loss

FastMap loss eliminates the effects of manually annotated vector points and constrains the model with more appropriate point-to-line connections. As illustrated in the bottom right corner of Figure 2, it consists of five losses, points-points loss, point-line loss, auxiliary line loss, classification loss, and heatmap loss.

#### 3.3.1. Points-Points Loss

Considering that the start and end points represent the length of the whole instance, which is different from other points on the line. Therefore, we use a hybrid supervised strategy to introduce points-points loss  $L_{pp}$  for the start and end points. By calculating the distance between the start and end points of the predicted instance to the start and end points of the ground truth instance, the model can better constrain the overall length of the map instance. This approach ensures that the model accurately captures the spatial extent of the map instances, enhancing the precision and reliability of the reconstructed map.

$$L_{pp} = \sum_{i=0}^{n-1} \text{dis}(p_{i,j}, gt_{i,j}), j = 0, m - 1. \quad (8)$$

Where  $\text{dis}()$  represents the L1 distance between the predicted point and the ground truth point. However, in closed map elements (such as pedestrian crossing), there is no concept of start and end points. Therefore, when calculating the loss for such closed map elements, the points-points loss  $L_{pp}$  is not considered.

#### 3.3.2. Points-Line Loss

Points in map instances often exhibit highly similar features. Forcibly fitting predicted points to ground truth points creates output redundancy, which is detrimental to model learning. For this reason, this paper proposes a line-constrained loss function (Point-Line Loss), which employs

point-to-line geometric constraints instead of the point-by-point matching mechanism. The Point-Line loss  $L_{pl}$  is expressed as follows:

$$L_{pl} = \sum_{i=0}^{n-1} \sum_{j=1}^{m-2} \text{abs} \left( \frac{(p_{i,j,x} - gt_{i,j-1,x})(gt_{i,j,x} - gt_{i,j-1,x})}{\sqrt{(gt_{i,j,y} - gt_{i,j-1,y})^2 + (gt_{i,j,x} - gt_{i,j-1,x})^2}} - \frac{(p_{i,j,y} - gt_{i,j-1,y})(gt_{i,j,y} - gt_{i,j-1,y})}{\sqrt{(gt_{i,j,y} - gt_{i,j-1,y})^2 + (gt_{i,j,x} - gt_{i,j-1,x})^2}} \right), \quad (9)$$

$gt_{i,j,x}$  and  $gt_{i,j,y}$  denote the x and y coordinates of the j-th point within the i-th instance in the ground truth, while  $p_{i,j,x}$  and  $p_{i,j,y}$  represent the x and y coordinates of the j-th point within the i-th instance in the prediction. The variable n indicates the total number of instances and m specifies the number of points contained within each instance.

#### 3.3.3. Auxiliary Line Loss

The auxiliary line loss  $L_{al}$  constrains the predicted point to lie within the interval defined by the endpoints of its corresponding vector by calculating the sum of the distances between the current predicted point and the two endpoints of the vector. This prevents the predicted point from deviating onto the extension of the line segment. Its expression is as follows:

$$L_{al} = \sum_{i=0}^{n-1} \sum_{j=1}^{m-2} \text{dis}(p_{i,j} - gt_{i,j}) + \text{dis}(p_{i,j} - gt_{i,j-1}). \quad (10)$$

#### 3.3.4. Heatmap Loss

We employ focal loss to assist the model capture map information in the BEV features. To better focus on global map elements, FastMap incorporates a Gaussian heatmap weight  $W_{gauss}$  in the calculation of the heatmap loss, which enhances the retention of distant information.

$$W_{gauss} = (1.0 - \exp(-\frac{x^2 + y^2}{2\sigma_x\sigma_y}))\alpha_{gauss} + 1.0, \quad (11)$$

$\alpha_{gauss}$  represents the Gaussian weight sparsity. x and y denote the coordinates of the current pixel. The terms  $\alpha_x = \frac{h}{\beta_{gauss}}$  and  $\alpha_y = \frac{w}{\beta_{gauss}}$  define the standard deviations of the Gaussian distribution, where larger  $\beta_{gauss}$  results in smaller variances. h and w correspond to the height and width of the heatmap. The weight of the Gaussian heatmap increases gradually from the center to the periphery: it reaches 1.0 at the center of the heatmap and reaches  $\alpha_{gauss} + 1.0$  at the farthest edge. The heatmap loss is ex-

Table 1. Comparison with state-of-the-art methods on the nuScenes validation set. R18, R50, and Effi-B0 denote ResNet18 [7], ResNet50 [7], and EfficientNet-B0 [9] architectures, respectively. R18, R50 and Effi-B0 are all initialized with ImageNet [5] pre-trained weights. FPS (Frames Per Second) metrics are measured on the same machine equipped with an NVIDIA GeForce RTX 3090.

Model	Backbone	Epoch	AP_div	AP_ped	AP_bou	mAP	AP_div	AP_ped	AP_bou	mAP	FPS
			[0.2m,0.5m,1.0m]				[0.5m,1.0m,1.5m]				
HDMaPNet [10]	Effi-B0	30	28.3	7.1	32.6	22.7	21.7	14.4	33.0	23.0	1.6
MapTR [13]	R50	24	30.7	23.2	28.2	27.3	51.5	46.3	53.1	50.3	15.1
PivotNet [6]	R50	24	42.9	34.8	39.3	39.0	58.8	53.8	59.6	57.4	10.4
BeMapNet [19]	R50	24	46.9	39.0	37.8	41.3	62.3	57.7	59.4	59.8	7.0
MapQR [17]	R50	24	49.9	38.6	41.5	43.3	68.0	63.4	67.7	66.4	12.8
HybriMap [27]	R50	24	45.7	38.1	42.1	41.9	65.9	63.0	67.2	65.4	9.9
PrevPredMap [18]	R50	24	-	-	-	-	66.9	64.5	67.6	66.3	13.1
MGMaP [15]	R50	110	54.5	42.1	37.4	44.7	67.6	64.4	67.7	66.5	11.1
PriorMapNet [22]	R50	24	-	-	-	-	69.0	64.0	68.2	67.1	11.7
MapTRv2 [14]	R18	110	-	-	-	-	55.1	46.9	54.9	52.3	16.3
MapTRv2 [14]	R50	24	40.0	35.4	36.3	37.2	62.4	59.8	62.4	61.5	14.1
FastMap-tiny	R18	24	37.4	29.5	34.4	33.8	57.4	53.2	59.6	56.7	23.3
FastMap-base	R50	24	41.1	35.2	38.0	38.1	62.5	59.9	63.6	62.0	19.8
FastMap-large	R50	24	54.5	44.6	41.6	46.8	69.1	65.5	69.7	68.1	14.8

Table 2. Comparisons with state-of-the-art methods on Argoverse2 val set. All models listed in the table were trained for 6 epochs.

Model	Backb.	$AP_{div}$	$AP_{ped}$	$AP_{bou}$	mAP
MapTR [13]	R50	50.6	60.7	61.2	57.4
MapQR [17]	R50	71.2	65.3	67.9	68.2
HIMaP [29]	R50	69.5	69.0	70.3	69.6
MapTRv2 [14]	R50	72.1	62.9	67.1	67.4
FastMap-tiny	R18	67.0	60.5	63.8	63.8
FastMap-base	R50	71.9	63.8	68.2	68.0
FastMap-large	R50	72.5	69.3	72.1	71.3

pressed as follows:

$$L_{focal} = \sum_{x=0}^h \sum_{y=0}^w (H_{x,y}^p, H_{x,y}^{gt}), \quad (12)$$

where  $H_{x,y}^p$  denotes the predicted of heatmap pixel value and  $H_{x,y}^{gt}$  denotes the ground truth of heatmap pixel value.

### 3.3.5. Total Loss

In the first stage, the coarse-grained feature  $F_{coarse}$  is crucial for rapid convergence of the model. To obtain more accurate reference point positions, we also calculate the loss between the reference points generated in the first stage and the ground truth instances. The overall loss  $L_{total}$  is expressed as follows:

$$\begin{aligned} L_{total} = & \gamma(\alpha_{cls}L_{cls}^1 + \alpha_{pl}L_{pl}^1 + \alpha_{pp}L_{pp}^1 + \alpha_{al}L_{al}^1) \\ & + \beta(\alpha_{cls}L_{cls}^2 + \alpha_{pl}L_{pl}^2 + \alpha_{pp}L_{pp}^2 + \alpha_{al}L_{al}^2) \\ & + \alpha_{heat}L_{heat}, \end{aligned} \quad (13)$$

where  $\gamma$  denotes the weight of the overall loss in the first stage and  $\beta$  represents the weight of the overall loss in the

second stage. The weights for classification loss, point-line loss, points-points loss, auxiliary line loss and heatmap loss are denoted by  $\alpha_{cls}$ ,  $\alpha_{pl}$ ,  $\alpha_{pp}$ ,  $\alpha_{al}$ , and  $\alpha_{heat}$  respectively.

## 4. Experiments

In this section, we first introduce the experimental setup in Section 4.1. In Section 4.2, we report the comparative experimental results. In Section 4.3 we perform extensive ablation experiments to verify the effectiveness of the individual modules. We further analyze the model to demonstrate its superior performance in Section 4.4.

### 4.1. Experimental setup

#### 4.1.1. Implementation Details

We use ResNet50 [7] as the image backbone network for FastMap-base and FastMap-large, and ResNet18 [7] for FastMap-tiny. The optimizer is AdamW with a weight decay of 0.01. The batch size is 32, and the training is carried out using 8 NVIDIA H100 GPUs. For inference validation, a single NVIDIA GeForce RTX 3090 GPU is used to ensure consistent conditions with other models when testing FPS. We employ 6 epochs of heatmap pre-training (using only Heatmap Loss) and 24 epochs of regular training, with an initial learning rate of  $8e^{-4}$  and cosine decay. The number of decoder layers is set to 1 for FastMap-tiny and FastMap-base, and to 6 for FastMap-large. For the nuScenes and Argoverse2 datasets, parameters such as instance queries, point query numbers, and input image sizes follow the settings of MapTRv2 [14]. In FastMap Loss, the weights  $\alpha_{cls}$ ,  $\alpha_{pl}$ ,  $\alpha_{pp}$ ,  $\alpha_{al}$ , and  $\alpha_{heat}$  are set to 2.0, 2.5, 2.5, 2.5 and 0.6 respectively. The  $\alpha_{gauss}$  for heatmap loss is set to 0.8. Loss weight  $\alpha$  and loss weight  $\beta$  are set to 0.5 and 1.0, re-

Table 3. The mAP, inference time, and parameter count of MapTR [13] and FastMap-tiny. Where decoder=n indicates the use of n layer of decoder. When reporting the inference time, we have additionally detailed the FGCA, CGCA, and CSM within the decoder.

Model	mAP	FGCA	CGCA	CSM	Decoder	Parameter
MapTR(decoder=1)	29.1	4.1ms	-	-	6.2ms	40.6M
MapTR(decoder=2)	42.4	8.1ms	-	-	10.3ms	41.8M
MapTR(decoder=6)	50.3	24.0ms	-	-	26.2ms	46.7M
FastMap-tiny	56.7	2.5ms	2.9ms	1.5ms	8.1ms	41.5M

Table 4. Ablation study report for each module. FGCA represents the Fine-Grained Cross-Attention, CGCA denotes the Coarse-Grained Cross-Attention, CSM stands for the Circular Sampling Method, GHW represents the Gaussian heatmap weight, and HP denotes the heatmap pretrain.

FGCA	CGCA	FastMap	CSM	GHW	HP	$AP_{div}$	$AP_{ped}$	$AP_{bou}$	mAP
✓	✗	✗	✗	✗	✗	30.2	20.8	36.3	29.1
✓	✓	✗	✗	✗	✗	57.5	43.8	55.5	52.3 (+23.2)
✓	✓	✓	✗	✗	✗	59.9	49.6	59.5	56.3 (+4.0)
✓	✓	✓	✓	✗	✗	58.2	55.1	62.6	58.6 (+2.3)
✓	✓	✓	✓	✓	✗	62.0	56.7	62.3	60.4 (+1.8)
✓	✓	✓	✓	✓	✓	62.5	59.9	63.6	62.0 (+1.6)

spectively. The total number of sampling points  $M$  is set to 3500, and the Gaussian dilation kernel size is set to 3.

#### 4.1.2. Evaluation Dataset

We evaluated our method on the mainstream nuScenes dataset [2]. The nuScenes dataset contains 2D city-level global vectorized maps and 1000 scenes, with each scene lasting approximately 20 seconds. Key samples are annotated at a frequency of 2Hz. Each sample includes RGB images from six cameras, covering a 360-degree horizontal Field Of View (FOV) around the ego vehicle. To further demonstrate the robustness of the model, we performed experiments on the Argoverse2 dataset [24], which contains 1000 logs. Each log provides 15 seconds of 20Hz RGB images from 7 cameras and log-level 3D vectorized maps.

#### 4.1.3. Evaluation metrics

We set the perception range for the X-axis to [-15.0m, 15.0m] and for the Y-axis to [-30.0m, 30.0m], using Average Precision (AP) to evaluate the quality of map construction. The chamfer distance is used to determine whether the predicted values match the ground truth (GT). We calculate the AP at multiple chamfer distance thresholds and then take the average of all thresholds as the final AP metric. In the experiments, the thresholds are divided into two groups: [0.2, 0.5, 1.0] and [0.5, 1.0, 1.5].

### 4.2. Comparison experiments

#### 4.2.1. nuScenes

Table 1 reports the performance metrics of FastMap-tiny, FastMap-base, and FastMap-large on the nuScenes dataset. FastMap-tiny, which uses a small backbone network (ResNet18), significantly outperforms its baseline (MapTR)

in both model accuracy and inference speed. Its precision improved by 6.4 mAP compared to MapTR, while the inference speed increased significantly by 54.3%. FastMap-base, while improving 0.5 mAP over MapTR, achieved a substantial 40.4% increase in inference speed. FastMap-large achieved the best performance with a slightly higher inference speed than the baseline, reaching 68.1 mAP, demonstrating that heatmap initialization can still ensure the model’s upper limit. The excellent performance of FastMap is also verified in the more strict evaluation annotation (thresholds of [0.2, 0.5, 1.0]), where its AP has a greater improvement compared to the baseline, indicating that FastMap produces more detailed map instances.

#### 4.2.2. Argoverse2

Meanwhile, Table 2 shows the results of our framework evaluated on the Argoverse2 dataset. FastMap also demonstrated its outstanding performance here. FastMap-tiny improved by 6.4 mAP compared to MapTR, FastMap-base improved by 0.6 mAP compared to MapTRv2, and FastMap-large achieved 71.3 mAP on the Argoverse2 dataset.

### 4.3. Ablation experiments

Table 3 reports the mAP, inference time, and parameters for MapTR and FastMap-base. It can be seen that FastMap is fully ahead of MapTR in terms of mAP, computing speed and number of model parameters, and its decoder speed is improved by 17.1 ms compared to MapTR while maintaining the performance improvement of 6.4 mAP. FGCA in FastMap reduces two MHAs compared to MapTRv2 thus reducing the single-layer elapsed time by 1.6 ms.

Table 4 reports the ablation experiments for each module. We used MapTR with 1 decoder layer as the baseline.

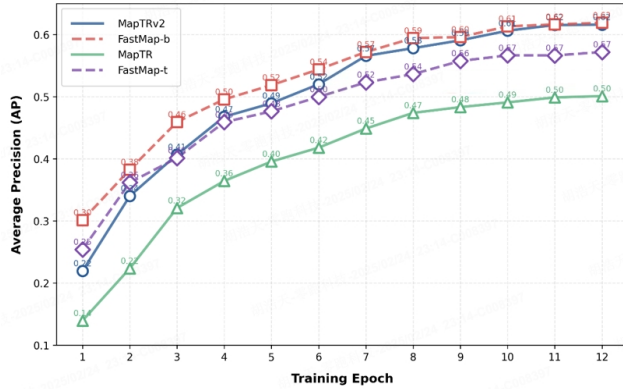


Figure 4. AP rise line graphs for MapTR, MapTRv2, FastMap-tiny, and FastMap-base. x-axis denotes the current epoch and y-axis denotes the corresponding AP.

Adding CGCA significantly improved the model accuracy to 52.3 mAP, indicating that initializing map queries using ROI regions effectively alleviates the redundancy issue in the decoder structure. FastMap Loss improved the model by 4.0 mAP, proving that the point-to-line loss effectively mitigates the feature ambiguity caused by manual annotation. Adding CSM and heatmap weight loss further improved the model by 2.3 mAP and 1.8 mAP, respectively, demonstrating that these strategies effectively enhance the recall rate in the first stage of the encoder.

#### 4.4. Analysis

As illustrated in Figure 4, due to the more accurate location of the reference point, FastMap-base demonstrates a higher convergence rate relative to MapTRv2. In particular, at the first epoch, a disparity of 8.1% in mAP is observed between the two models. Furthermore, the most lightweight model FastMap-tiny surpasses MapTRv2 in terms of AP during the initial training stage, which underscores the significant improvement in model convergence speed achieved by FastMap.

Table 5. Comparison results of ACD/ARD/AJP between FastMap, MapTR and MapTRv2. ↓ indicates that the lower the value the better the performance.

Model	MapTR	MapTRv2	FastMap-t	FastMap-b
ACD ↓	0.597	0.560	0.551	0.505
ARD ↓	7.866	5.950	6.312	5.286
AJP ↓	6.76	4.53	5.12	4.08

ACD refers to the average chamfer distance between each positive sample and the corresponding ground truth instance. ARD measures the average radian distance within an instance, calculated as the sum of the radians of the angles between consecutive line segments in each positive

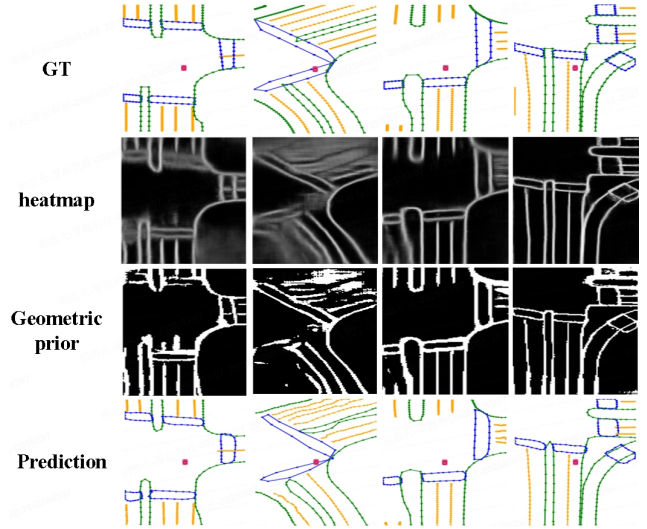


Figure 5. Heatmap ground truth, heatmap, geometric priors and prediction visualization results.

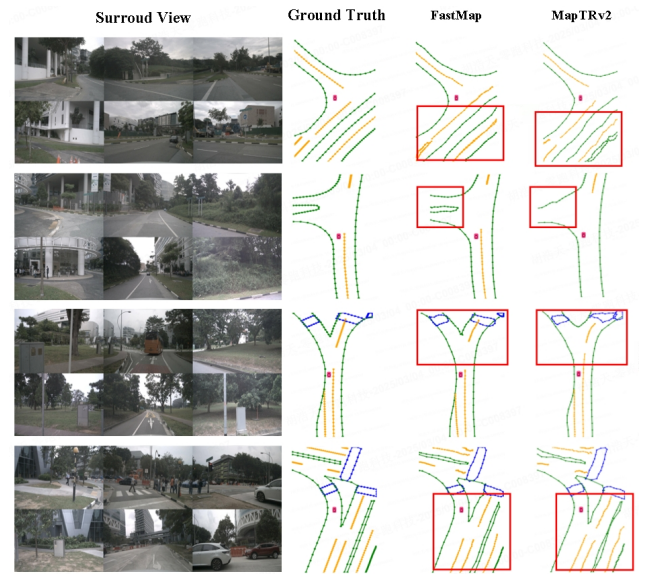


Figure 6. Visualization results of FastMap and MapTRv2 in nuScenes dataset.

sample and the ground truth segments. AJP represents the average number of jitter points within an instance, defined as points where the angle between adjacent line segments exceeds  $30^\circ$ , while the corresponding true point maintains an angle below  $5^\circ$ . These metrics are systematically compared in Table 5.

Figure 5 illustrates that the predicted heatmap performs well even in intersections, indicating that inaccurate heatmap prediction does not become a bottleneck for

FastMap. In addition, CRM evenly samples foreground prior across all regions, ensuring that the geometric prior maintain a high recall rate. As shown in Figure 6, the FastMap output vectors are smoother and effectively mitigate the problem of missed detections by the model.

## 5. Conclusions

The Proposed FastMap is an end-to-end framework designed for efficient online vector mapping. It utilizes heatmap initialization for map queries to address the issue of redundant stacking in the decoder and to accelerate the model's convergence speed. Extensive experiments have shown that our proposed method can achieve efficient performance on nuScenes and Argoverse2 datasets. We hope that FastMap can be an effective paradigm for efficient online vector maps that can provide good performance in addressing resource-limited environments. And to advance downstream tasks such as motion prediction and planning.

## References

- [1] Xuyang Bai, Zeyu Hu, Xinge Zhu, Qingqiu Huang, Yilun Chen, Hongbo Fu, and Chiew-Lan Tai. Transfusion: Robust lidar-camera fusion for 3d object detection with transformers. In *Proceedings of the IEEE/CVF conference on computer vision and pattern recognition*, pages 1090–1099, 2022. 1, 2
- [2] Holger Caesar, Varun Bankiti, Alex H Lang, Sourabh Vora, Venice Erin Liang, Qiang Xu, Anush Krishnan, Yu Pan, Giancarlo Baldan, and Oscar Beijbom. nuscenes: A multi-modal dataset for autonomous driving. In *Proceedings of the IEEE/CVF conference on computer vision and pattern recognition*, pages 11621–11631, 2020. 2, 7
- [3] Nicolas Carion, Francisco Massa, Gabriel Synnaeve, Nicolas Usunier, Alexander Kirillov, and Sergey Zagoruyko. End-to-end object detection with transformers. In *European conference on computer vision*, pages 213–229. Springer, 2020. 1, 2
- [4] Jiacheng Chen, Yuefan Wu, Jiaqi Tan, Hang Ma, and Yasutaka Furukawa. Maptracker: Tracking with strided memory fusion for consistent vector hd mapping. In *European Conference on Computer Vision*, pages 90–107. Springer, 2024. 1
- [5] Jia Deng, Wei Dong, Richard Socher, Li-Jia Li, Kai Li, and Li Fei-Fei. Imagenet: A large-scale hierarchical image database. In *2009 IEEE conference on computer vision and pattern recognition*, pages 248–255. Ieee, 2009. 6
- [6] Wenjie Ding, Limeng Qiao, Xi Qiu, and Chi Zhang. Pivotnet: Vectorized pivot learning for end-to-end hd map construction. In *Proceedings of the IEEE/CVF International Conference on Computer Vision*, pages 3672–3682, 2023. 6
- [7] Kaiming He, Xiangyu Zhang, Shaoqing Ren, and Jian Sun. Deep residual learning for image recognition. In *Proceedings of the IEEE conference on computer vision and pattern recognition*, pages 770–778, 2016. 6
- [8] Haotian Hu, Fanyi Wang, Yaonong Wang, Laifeng Hu, Jingwei Xu, and Zhiwang Zhang. Admap: Anti-disturbance framework for reconstructing online vectorized hd map. In *European Conference on Computer Vision*. Springer, 2024. 1
- [9] Brett Koonce. Efficientnet. In *Convolutional neural networks with swift for Tensorflow: image recognition and dataset categorization*, pages 109–123. Springer, 2021. 6
- [10] Qi Li, Yue Wang, Yilun Wang, and Hang Zhao. Hdmapnet: An online hd map construction and evaluation framework. In *2022 International Conference on Robotics and Automation (ICRA)*, pages 4628–4634. IEEE, 2022. 1, 6
- [11] Siyu Li, Jiacheng Lin, Hao Shi, Jiaming Zhang, Song Wang, You Yao, Zhiyong Li, and Kailun Yang. Dtclmapper: Dual temporal consistent learning for vectorized hd map construction. *IEEE Transactions on Intelligent Transportation Systems*, 2024.
- [12] Toyota Li. Mapnext: Revisiting training and scaling practices for online vectorized hd map construction. *arXiv preprint arXiv:2401.07323*, 2024. 1
- [13] Bencheng Liao, Shaoyu Chen, Xinggong Wang, Tianheng Cheng, Qian Zhang, Wenyu Liu, and Chang Huang. Maptr: Structured modeling and learning for online vectorized hd map construction. In *International Conference on Learning Representations*, 2023. 1, 3, 6, 7
- [14] Bencheng Liao, Shaoyu Chen, Yunchi Zhang, Bo Jiang, Qian Zhang, Wenyu Liu, Chang Huang, and Xinggong Wang. Maptrv2: An end-to-end framework for online vectorized hd map construction. *International Journal of Computer Vision*, pages 1–23, 2024. 1, 6
- [15] Xiaolu Liu, Song Wang, Wentong Li, Ruizi Yang, Junbo Chen, and Jianke Zhu. Mgmmap: Mask-guided learning for online vectorized hd map construction. In *Proceedings of the IEEE/CVF Conference on Computer Vision and Pattern Recognition*, pages 14812–14821, 2024. 6
- [16] Yicheng Liu, Tianyuan Yuan, Yue Wang, Yilun Wang, and Hang Zhao. Vectormapnet: End-to-end vectorized hd map learning. In *International Conference on Machine Learning*, pages 22352–22369. PMLR, 2023. 2
- [17] Zihao Liu, Xiaoyu Zhang, Guangwei Liu, Ji Zhao, and Ningyi Xu. Leveraging enhanced queries of point sets for vectorized map construction. In *European Conference on Computer Vision*, pages 461–477. Springer, 2024. 6
- [18] Nan Peng, Xun Zhou, Mingming Wang, Xiaojun Yang, Songming Chen, and Guisong Chen. Prevpredmap: Exploring temporal modeling with previous predictions for online vectorized hd map construction. *arXiv preprint arXiv:2407.17378*, 2024. 6
- [19] Limeng Qiao, Wenjie Ding, Xi Qiu, and Chi Zhang. End-to-end vectorized hd-map construction with piecewise bezier curve. In *Proceedings of the IEEE/CVF Conference on Computer Vision and Pattern Recognition*, pages 13218–13228, 2023. 1, 6
- [20] Tixiao Shan and Brendan Englot. Lego-loam: Lightweight and ground-optimized lidar odometry and mapping on variable terrain. In *2018 IEEE/RSJ International Conference on Intelligent Robots and Systems (IROS)*, pages 4758–4765. IEEE, 2018. 1

- [21] Tixiao Shan, Brendan Englot, Drew Meyers, Wei Wang, Carlo Ratti, and Daniela Rus. Lio-sam: Tightly-coupled lidar inertial odometry via smoothing and mapping. In *2020 IEEE/RSJ international conference on intelligent robots and systems (IROS)*, pages 5135–5142. IEEE, 2020. 1
- [22] Rongxuan Wang, Xin Lu, Xiaoyang Liu, Xiaoyi Zou, Tongyi Cao, and Ying Li. Priormapnet: Enhancing online vectorized hd map construction with priors. *arXiv preprint arXiv:2408.08802*, 2024. 6
- [23] Shuo Wang, Fan Jia, Weixin Mao, Yingfei Liu, Yucheng Zhao, Zehui Chen, Tiancai Wang, Chi Zhang, Xiangyu Zhang, and Feng Zhao. Stream query denoising for vectorized hd-map construction. In *European Conference on Computer Vision*, pages 203–220. Springer, 2024. 1
- [24] Benjamin Wilson, William Qi, Tanmay Agarwal, John Lambert, Jagjeet Singh, Siddhesh Khandelwal, Bowen Pan, Ratnesh Kumar, Andrew Hartnett, Jhony Kaesemodel Pontes, et al. Argoverse 2: Next generation datasets for self-driving perception and forecasting. *arXiv preprint arXiv:2301.00493*, 2023. 2, 7
- [25] Kuang Wu, Sulei Nian, Can Shen, Chuan Yang, and Zhanbin Li. Lgmap: Local-to-global mapping network for online long-range vectorized hd map construction. *arXiv preprint arXiv:2406.13988*, 2024. 1
- [26] Zhuyu Yao, Jiangbo Ai, Boxun Li, and Chi Zhang. Efficient detr: improving end-to-end object detector with dense prior. *arXiv preprint arXiv:2104.01318*, 2021. 1, 2
- [27] Chi Zhang, Qi Song, Feifei Li, Yongquan Chen, and Rui Huang. Hybrimap: Hybrid clues utilization for effective vectorized hd map construction. *arXiv preprint arXiv:2404.11155*, 2024. 6
- [28] Xiaoyu Zhang, Guangwei Liu, Zihao Liu, Ningyi Xu, Yunhui Liu, and Ji Zhao. Enhancing vectorized map perception with historical rasterized maps. In *European Conference on Computer Vision*, pages 422–439. Springer, 2024. 3
- [29] Yi Zhou, Hui Zhang, Jiaqian Yu, Yifan Yang, Sangil Jung, Seung-In Park, and ByungIn Yoo. Himap: Hybrid representation learning for end-to-end vectorized hd map construction. In *Proceedings of the IEEE/CVF Conference on Computer Vision and Pattern Recognition*, pages 15396–15406, 2024. 3, 6
- [30] Xizhou Zhu, Weijie Su, Lewei Lu, Bin Li, Xiaogang Wang, and Jifeng Dai. Deformable detr: Deformable transformers for end-to-end object detection. *arXiv preprint arXiv:2010.04159*, 2020. 1